Correlation-Pattern-Based Orbital Angular Momentum Entanglement Measurement Through Neural Networks

Jiaxian Zhao(赵嘉娴)[1†], Zhifeng Liu(刘志峰)[1†], Chenghou Tu(涂成厚)[1], Yongnan Li(李勇男)[1*], and Hui-Tian Wang(王慧田)[2*]

[1]*Key Laboratory of Weak-Light Nonlinear Photonics and School of Physics, Nankai University, Tianjin 300071, China*
[2]*National Laboratory of Solid State Microstructures, School of Physics, and Collaborative Innovation Center of Advanced Microstructures, Nanjing University, Nanjing 210093, China*

(Received 12 January 2025; accepted manuscript online 24 February 2025)

High-dimensional (HD) entanglement of photonic orbital angular momentum (OAM) is pivotal for advancing quantum communication and information processing, but its characterization remains significant challenges due to the complexity of quantum state tomography and experimental limitations such as low photon counts caused by losses. Here, we propose a pre-trained physics-informed neural network (PTPINN) framework that enables efficient and rapid reconstruction of HD-OAM entangled states under low photon counts. Experimental results show that the fidelity of five-dimensional OAM entanglement reaches $F = 0.958 \pm 0.010$ even with an exposure time as short as 50 ms. This highlights the capability of PTPINN to achieve high-precision quantum state reconstruction with limited photons, owing to its innovative designs, thus overcoming the reliance on high photon counts typical of traditional methods. Our method provides a practical and scalable solution for high-fidelity characterization of HD-OAM entanglement in environments with low photon numbers and high noise, paving the way for robust long-distance quantum information transmission.

DOI: 10.1088/0256-307X/42/3/030205 CSTR: 32039.14.0256-307X.42.3.030205

Introduction. Quantum entanglement based on orbital angular momentum (OAM) not only expands the dimensionality of the Hilbert space for encoding more information,[1–8] but also significantly enhances the noise resistance and robustness of systems.[9–12] However, characterizing high-dimensional (HD) OAM entanglement remains challenges, including numerous measurements, complex data processing, and time-consuming procedures.[13–21] This highlights the need for solutions that can efficiently and accurately characterize HD-OAM entanglement. Recently, a two-measurement, scanning-free tomography strategy employing an intensified charge-coupled device (ICCD) camera has significantly reduced the number of required measurements, simplifying quantum state tomography (QST).[22] However, due to the low quantum efficiency of the ICCD, accurate measurements of quantum states require long exposure time to obtain clear probability distributions. In addition, photon loss normally increases with the length of communication channel and cannot be compensated by amplification because of the quantum non-cloning theorem.[23–25] Consequently, the photon number received decreases dramatically, severely constraining the transmission and processing of quantum information. Therefore, efficiently characterizing quantum states with fewer photons presents a significant challenge for advancing quantum technologies.

In recent years, deep learning has garnered significant attention for its ability to handle large-scale data and complex problems.[26] It has been widely applied to data analysis and optimization in various fields, including phase retrieval,[27,28] structured light recognition,[29,30] and quantum information science.[31,32] In the characterization of entanglement, the deep learning has introduced innovative solutions for managing complex quantum systems.[33–38] However, conventional data-driven approaches, such as convolutional neural networks (CNNs), rely heavily on large labeled datasets to establish accurate mappings, which presents difficulty in data collection, generalization, and interpretability. These limitations require innovative approaches that combine data-driven methods with model-driven techniques that integrate physical models, to enhance processing speed, scalability, and adaptability.

Here we propose a pre-trained physics-informed neural network (PTPINN) for characterizing OAM entanglement under low-sampling conditions. By incorporating parameters from a pre-trained CNN trained on lower-dimensional entanglement data into the physics informed neural network (PINN),[39] this approach enhances the reconstruction accuracy of HD-OAM entanglement, while significantly reducing tomography time. We have validated the feasibility of this method through both simulation and experiment, demonstrating its ability to accurately reconstruct quantum state even under very low sampling counts.

†These authors contributed equally to this work.
*Corresponding author. Email: liyongnan@nankai.edu.cn; htwang@nju.edu.cn
© 2025 Chinese Physical Society and IOP Publishing Ltd. All rights, including for text and data mining, AI training, and similar technologies, are reserved.

This advancement is crucial for extending communication distances while ensuring efficient and reliable information transmission.

Model and Method. The spontaneous parametric down-conversion (SPDC) process is a primary mechanism for generating OAM entanglement,[40] which can be expressed as

$$|\psi\rangle = \sum_{l=-d}^{d} \alpha_l \exp(j\phi_l)|l\rangle_s|-l\rangle_i, \tag{1}$$

where $|l\rangle$ represents the Laguerre-Gaussian mode with a topological charge of l and a radial index being 0. The dimensionality of the entanglement is $D = 2d + 1$. The amplitudes α_l and phases ϕ_l of the terms $|l\rangle_s|-l\rangle_i$ are the entanglement parameters required to fully characterize the system. The amplitudes α_l satisfy the normalization condition of $\sum_{l=-d}^{d} \alpha_l^2 = 1$, and the phases ϕ_l are within a range of $\phi_l \in [0, 2\pi)$ and can set $\phi_0 = 0$ without loss of generality. According to the previously proposed two-measurement tomography using the ICCD,[22] the two measurements need to project the signal photons onto two superposition states $|\dot{\Psi}_s\rangle \propto \sum_{l=0}^{d} |l\rangle_s$ and $|\ddot{\Psi}_s\rangle \propto \sum_{l=-d}^{0} |l\rangle_s$, respectively. The corresponding idler photons then collapse into the following states

$$|\dot{\Psi}_i\rangle = \langle\dot{\Psi}_s|\psi\rangle \propto \sum_{l=0}^{d} \alpha_l \exp(j\phi_l)|-l\rangle_i, \tag{2a}$$

$$|\ddot{\Psi}_i\rangle = \langle\ddot{\Psi}_s|\psi\rangle \propto \sum_{l=-d}^{0} \alpha_l \exp(j\phi_l)|-l\rangle_i. \tag{2b}$$

We use the ICCD triggered by signal photons to detect idler photons and obtain joint probability distributions. By adjusting the exposure time of the ICCD, we control the number of photons measured by effectively setting the number of sampling points N. In this work, we develop a PTPINN algorithm model to directly extract the entanglement parameters α_l and ϕ_l from two measured patterns, enabling the reconstruction of OAM entangled states. As illustrated in Fig. 1, the proposed method consists of two main steps: using a pre-trained CNN model to obtain convolution parameters and employing a model-driven iterative process to determine the entanglement parameters. First, a dataset of probability patterns for OAM entanglement in lower dimension is used to train the CNN, allowing the network to learn the relationship between probability patterns and entanglement parameters. The pre-trained convolution parameters are then transferred to the PINN model and kept frozen, forming the PTPINN. Such an adjustment allows only the parameters in the fully connected layers to update during the iterative process, significantly reducing training time compared to the standard PINN, which initializes all parameters randomly. The probability pattern $I(\alpha, \phi)$ of the idler photons is input to the adjusted PTPINN model. The output values $\tilde{\alpha}_l$ and $\tilde{\phi}_l$ are then used to generate a simulated probability pattern $\tilde{I}(\tilde{\alpha}, \tilde{\phi})$ based on Eq. (2), serving as the physical model constraint. During training, the weights in the fully connected layers are iteratively updated to minimize the error between the measured pattern $I(\alpha, \phi)$ and the simulated pattern $\tilde{I}(\tilde{\alpha}, \tilde{\phi})$. As the error decreases, the network outputs converge toward the ideal entanglement parameters. Finally, the density matrix of the target state is reconstructed. Physical priors effectively constrain the solution space, guiding the network to generate physically valid quantum states with the desired characteristics while preventing non-physical solutions and improving reconstruction efficiency.

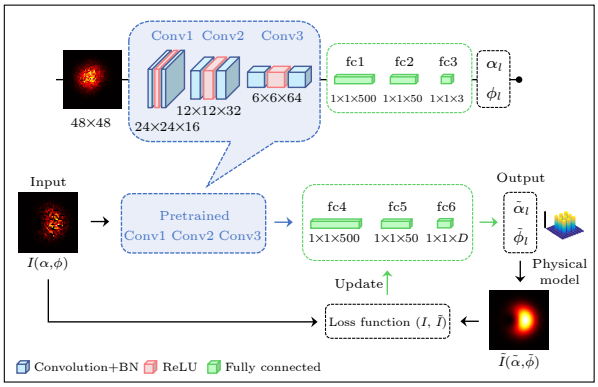

Fig. 1. Scheme of the data processing for characterizing HD-OAM entanglement under low sampling conditions using the PTPINN framework. The convolutional parameters pre-trained on a CNN are transferred to the PTPINN architecture. Under-sampled probability patterns of idler photons captured by the ICCD are processed by the PTPINN to extract the entanglement parameters.

The neural network architecture consists of a basic convolution layer, a regularization layer (Batch Normalization), a linear activation function (ReLU), and a fully connected layer. A sigmoid function is applied at the end of the PTPINN to constrain the entanglement parameters α_l and ϕ_l to the ranges [0,1] and [0,2π), respectively. The initial learning rate of the network is set to 1×10^{-4}, with a total of 100 optimization epochs. The Adam optimizer is employed throughout the optimization process to minimize the loss functions, including the mean-squared error (MSE) and the negative Pearson correlation coefficient (NPCC). The MSE measures the average squared difference between predicted and target values, ensuring precise predictions. The NPCC evaluates the linear correlation between predicted and target values, promoting alignment in their overall trends. All optimizations are implemented using PyTorch 1.13.1 and Python 3.9.7. The hardware setup includes an Intel(R) Xeon(R) Platinum 8378C CPU (3.60 GHz), 512 GB of RAM, and an NVIDIA GeForce RTX 4070 GPU.

Results and Discussion. To verify the accuracy and validity of the proposed model, we select two-photon 5D ($d = 2$) OAM entanglement as the target state for simulation

$$\begin{aligned}|\Psi\rangle \propto\ & 0.271\exp(j3\pi/2)|-2\rangle_s|2\rangle_i \\ & + 0.631\exp(j\pi/3)|-1\rangle_s|1\rangle_i \\ & + 0.451|0\rangle_s|0\rangle_i \\ & + 0.180\exp(j3\pi/4)|1\rangle_s|-1\rangle_i \\ & + 0.541\exp(j7\pi/5)|2\rangle_s|-2\rangle_i. \end{aligned} \tag{3}$$

The simulated probability patterns of the idler photons

were obtained by projecting signal photons onto the states $|\dot{\Psi}_s\rangle \propto |0\rangle_s + |1\rangle_s + |2\rangle_s$ and $|\ddot{\Psi}_s\rangle \propto |0\rangle_s + |-1\rangle_s + |-2\rangle_s$. To emulate experimental-like data, we apply a Monte Carlo sampling method to simulate the measurement results. Figure 2(a) shows the probability patterns for different numbers of sampling points N. The pattern for $N = \infty$ is directly obtained from the simulated probability distribution of the idler photons. As N increases from 10 to 100000, the Monte Carlo sampling results gradually converge to the $N = \infty$ case. For the pre-training model, we utilize convolution parameters from a 3D entanglement model trained on 500 randomly selected states, each sampled at 50 different rates. The Monte Carlo sampling results for various N were subsequently fed into the adjusted PTPINN for prediction. Figure 2(b) presents the loss curves during the iteration process. After approximately 20 iterations, the loss curves converge, indicating that the neural network successfully identifies a computational pattern $\tilde{I}$ that closely resembles the input pattern I. Although the overall shapes of $\tilde{I}$ and I are highly similar, pixel-level discrepancies persist. This prevents the loss curve from converging to zero, while stabilizes at a fixed value. The magnitude of the final loss value depends on N. The patterns generated with larger sampling numbers are closer to the true patterns, resulting in smaller loss values upon convergence. These loss values also provide an approximate estimate of the sampling points required for unknown under-sampled modes.

The reconstruction fidelity F can be calculated by $F = [\mathrm{Tr}(\sqrt{\sqrt{\rho}\sigma\sqrt{\rho}})]^2$, where ρ denotes the target quantum state and σ represents the quantum state reconstructed from the predicted values, as shown in Fig. 2(c).

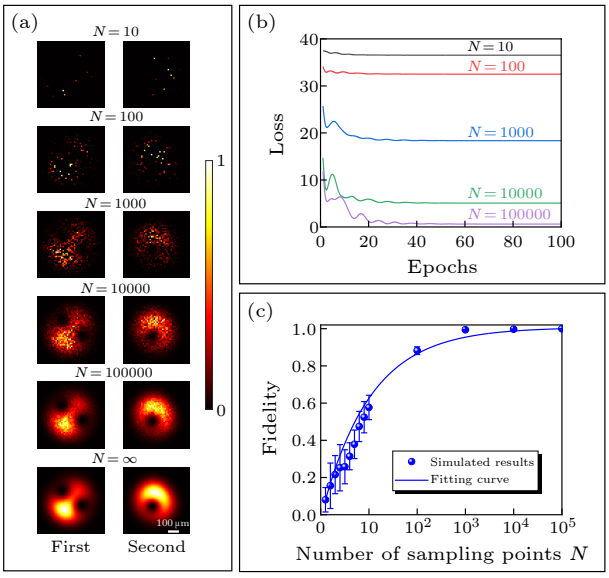

Fig. 2. Simulated results for 5D OAM entanglement. (a) Probability patterns of idler photons for different numbers of Monte Carlo sampling points. The image resolution is 48×48 pixels. "First" and "Second" indicate the results of the first and second measurements based on the two-measurement method. (b) Loss curves during training for patterns with varying sampling points. (c) Reconstructed fidelities across different number of sampling points.

When N is less than 10, the limited amount of available image data significantly increases recognition uncertainty, leading to greater fluctuations in fidelity due to insufficient statistical information for accurate quantum state reconstruction. As N increases, the sampling results more closely approximate the true patterns, allowing the model to converge more quickly and accurately. For $N = 10$, the reconstruction fidelity is approximately 0.6. At $N = 100$, the fidelity improves to 0.8, although it is still not fully satisfactory. For $N = 1000$, the fidelity after convergence reaches an impressive value of 0.993. This performance is comparable to the case of $N > 1000$, where additional sampling points provide only slight improvements in convergence speed and fidelity. The ability to achieve such high reconstruction accuracy through a modest number of sampling points significantly reduces the experimental workload and measurement time, making PTPINN an efficient solution for QST under limited sampling conditions.

We further experimentally verified the proposed method using 5D OAM entanglement as the target state [Fig. 3(a) and see "Experimental Details" Section for details]. According to the theory of SPDC under a Gaussian beam pump, the OAM entangled state should be

$$\begin{aligned}|\Psi\rangle \propto\ & 0.225|-2\rangle_s|2\rangle_i + 0.460|-1\rangle_s|1\rangle_i \\ & + 0.690|0\rangle_s|0\rangle_i \\ & + 0.460|1\rangle_s|-1\rangle_i + 0.225|2\rangle_s|-2\rangle_i. \end{aligned} \tag{4}$$

The signal photons are projected onto the superposition states of $|\dot{\Psi}_s\rangle \propto |0\rangle_s + |1\rangle_s + |2\rangle_s$ and $|\ddot{\Psi}_s\rangle \propto |0\rangle_s + |-1\rangle_s + |-2\rangle_s$, by using a spatial light modulator (SLM) loaded with corresponding holographic gratings. The probability patterns of the idler photons under various sampling conditions are obtained by adjusting the exposure time of the ICCD. As the exposure time decreases, the number of captured photons progressively diminished [Fig. 3(b)]. The probability patterns recorded under different exposure times are inputted into the PTPINN for prediction, and the corresponding reconstruction fidelities are calculated, as shown in Fig. 3(c). The predicted amplitude and phase values are displayed in Fig. 3(d). For sufficiently long exposure time (5 s), the fidelity reaches $F = 0.980 \pm 0.005$. Remarkably, even at an exposure time as short as 50 ms, the fidelity remains high at $F = 0.958 \pm 0.010$. However, when the exposure time is reduced to 10 ms, the limited number of captured photons results in a highly random distribution that poorly represents the true distribution of the target state. Based on the experimental parameters, our method requires only about 200 pairs of coincidence photons per measurement to achieve high-fidelity reconstruction of OAM entanglement, with just two measurements needed. In contrast, traditional tomography methods for 5D entanglement require at least 1000 pairs of coincidence photons per measurement and 625 measurements. This significant difference in photon requirements demonstrates that the PTPINN model can achieve high-precision state reconstruction under low-photon conditions, exhibiting strong noise resistance and robustness.

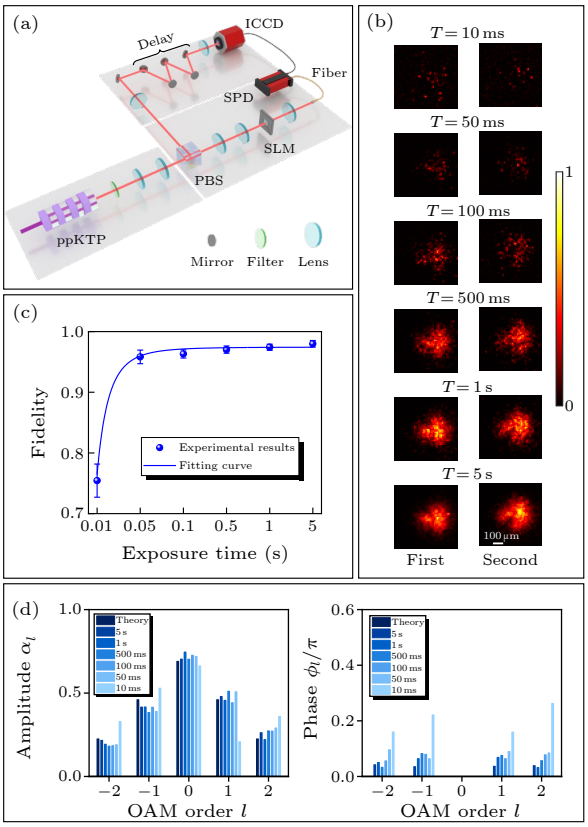

Fig. 3. Experiment on 5D OAM entanglement. (a) Experimental setup for the measurement of OAM entanglement. (b) Probability patterns of idler photons obtained at varying ICCD exposure times, with a resolution of 48×48 pixels. (c) Reconstruction fidelity at different exposure times. Error bars represent the mean values across 20 measurements. (d) Comparison of theoretical and experimental predictions of amplitudes α_l and phases ϕ_l.

We extend the predictive capability of our method to higher dimensions and compare its performance with a data-driven deep learning approach, namely, CNN. For the same sampling condition ($N = 1000$), the CNN exhibits poor performance as it struggles to generalize from low-dimensional entanglement training to higher-dimensional cases [Fig. 4(a)]. In contrast, the PTPINN is not constrained by the entanglement dimension and can generalize to predict entanglement states with dimensions higher than those used in pre-training, demonstrating strong scalability. Due to the pre-training, it achieves the higher fidelity and enhances the reconstruction performance by effectively capturing richer features and interrelationships through its model [Fig. 4(b)]. The fidelity improves as the dimensionality of the pre-training increases, further enhancing prediction accuracy. Figure 4(c) shows the dependence of measurement fidelity for seven-dimensional OAM entanglement on numbers of Monte Carlo sampling points N. As N decreases, the random errors introduced by under-sampling increase, leading to less stable predictions and greater deviations from the true values. The fidelities achieved by the CNN are $F = 0.981$ at $N = 100000$, while those achieved by the PTPINN are $F = 0.993$ at $N = 1000$. This indicates that the PTPINN can deliver better results with fewer sampling points,

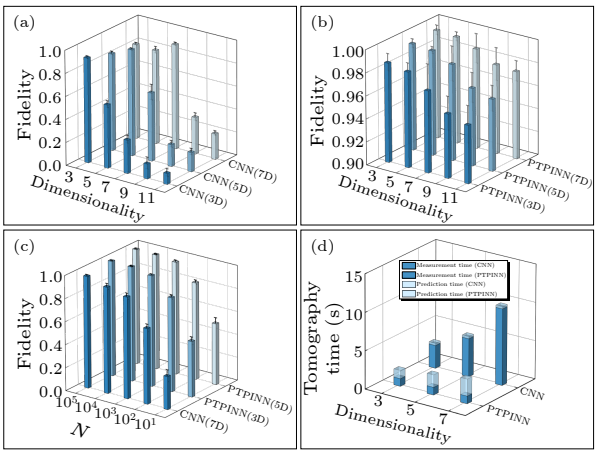

Fig. 4. Comparison between the CNN and PTPINN. Simulation results for entanglement prediction across different dimensions with a fixed number of sampling points ($N = 1000$), using (a) CNN, and (b) PTPINN. (c) Variation in reconstruction fidelities for seven-dimensional OAM entanglement under different sampling points. Error bars represent the average simulation results from 20 randomly selected states. (d) Total tomography time required experimentally by the CNN and PTPINN for different entangled dimensions. The CNN is trained individually for each predictive dimension to match the target, whereas the PTPINN uses pre-training on three-dimensional data for all predictions. Experimental fidelity results for entangled states in three, five, and seven dimensions are 0.978, 0.966, and 0.952 for the CNN, and 0.988, 0.978, and 0.967 for the PTPINN, respectively.

enabling accurate entanglement measurements with fewer received photons. The corresponding measurement times for the CNN and PTPINN in the experiment for different OAM entanglement dimensions are shown in Fig. 4(d). Although the CNN has the shorter prediction time, it requires longer exposure time to obtain clear probability patterns for extracting parameters of entangled states. The overall tomography time is still long and significantly increases with the dimension of quantum states. In contrast, the PTPINN does not require additional sampling data (i.e., received photon counts), resulting in a shorter overall tomography time that scales slowly with dimension. The PTPINN effectively addresses the challenge of decreasing fidelity caused by fewer photons received at higher dimensions, making it better suited for long-distance communication or complex quantum information processing.

Finally, we summarize the performances of both algorithms in Table 1. The CNN relies heavily on large labeled datasets and extensive computational resources, which limits its effectiveness for HD tasks. In contrast, the PTPINN combines the strengths of CNNs and PINNs, creating a hybrid approach that achieves high-quality, dimension-independent QST. After a one-time pre-training stage, PTPINN enables quantum state reconstruction across different dimensions, making it overall more efficient than other machine learning-based methods and traditional QST. Moreover, with its lower sampling requirements and faster tomography time, the PTPINN offers an efficient and scalable solution for characterizing HD-OAM entanglement.

Table 1. Performance comparison of the two algorithms.

	CNN	PTPINN
Physical model	None	Projection measurement
Training dataset	Large	Small
Threshold of N for the same high fidelity	$N \geq 10^5$	$N \geq 10^3$
Predictable range of dimensions	Constrained	Unlimited
HD scalability	Limited	Strong
Overall tomography time	Long	Short

Conclusion. In this work, we have proposed and validated the PTPINN for the efficient characterization of HD-OAM entangled states, combining the data-driven feature extraction capabilities of CNNs with the physics-constrained predictive power of PINNs. Under conditions of extremely low photon counts, auxiliary enhancement methods or alternative algorithms may be necessary to further improve performance. The PTPINN can transfer features learned from low dimensional pre training to HD tasks, ensuring its adaptability to different sampling conditions and any dimension, highlighting its flexibility and scalability. Both numerical simulations and experimental results demonstrate that the PTPINN achieves superior reconstruction fidelity with significantly fewer sampling points, thereby substantially reducing the overall tomography time. Additionally, the PTPINN can be extended to other spatial mode families, including Bessel-Gaussian,[41] Ince-Gaussian,[42] and Hermite-Gaussian[43] modes. Replacing the ICCD with a superconducting CCD[44] could further enhance measurement speed and efficiency. Our work introduces a novel and robust approach to QST, addressing the growing demands of HD quantum systems and paving the way for more practical and efficient quantum information processing techniques.

Experimental Details. The OAM entangled photon pairs are created in the SPDC process using a 10 mm-long type-II nonlinear crystal (PPKTP). A 405-nm continuous wave diode laser, operating at approximately 4.5 mW, is used to pump the crystal, generating photon pairs at a wavelength of 810 nm. A narrow bandwidth interference filter allows light at 810 nm to pass through while reflecting the 405 nm pump light. A polarization beam splitter separates the signal and idler photons into two distinct paths. By loading blazed gratings onto the SLM, the signal photons are projected into the desired OAM superposition states and detected using a pigtailed single photon avalanche detector (SPAD). Simultaneously, the ICCD is triggered to record the probability distribution of the idler photons, correlated with the signal photons. The ICCD triggering mechanism introduces an electronic delay of approximately 70 ns, requiring an additional spatial delay of about 22 m before the ICCD. The probability recorded by the ICCD camera is expressed in counts per pixel, which is linearly related to the number of detected photons.

Acknowledgements. This work was supported by the National Natural Science Foundation of China (12234009, 12474328, 12074196, 11922406, and 12074197).

References

[1] Wang X L, Cai X D, Su Z E, Chen M C, Wu D, Li L, Liu N L, Lu C Y, and Pan J W 2015 *Nature* **518** 516
[2] Kong L J, Liu R, Qi W R, Wang Z X, Huang S Y, Wang Q, Tu C, Li Y, and Wang H T 2019 *Sci. Adv.* **5** eaat9206
[3] Malik M, Erhard M, Huber M, Krenn M, Fickler R, and Zeilinger A 2016 *Nat. Photonics* **10** 248
[4] Liu S, Lv Y, Wang X, Wang J, Lou Y, and Jing J 2024 *Phys. Rev. Lett.* **132** 100801
[5] Hu X M, Guo Y, Liu B H, Huang Y F, Li C F, and Guo G C 2018 *Sci. Adv.* **4** eaat9304
[6] Huang S Y, Gao J, Ren Z C, Cheng Z M, Zhu W Z, Xue S T, Lou Y C, Liu Z F, Chen C, Zhu F, Yang L P, Wang X L, and Wang H T 2024 *Chin. Phys. Lett.* **41** 074205
[7] Zhao S M, Gong L Y, Li Y Q, Yang H, Sheng Y B, and Cheng W W 2013 *Chin. Phys. Lett.* **30** 060305
[8] Liu S, Lou Y, and Jing J 2020 *Nat. Commun.* **11** 3875
[9] Erhard M, Fickler R, Krenn M, and Zeilinger A 2018 *Light Sci. Appl.* **7** 17146
[10] He C, Shen Y, and Forbes A 2022 *Light Sci. Appl.* **11** 205
[11] Ecker S, Bouchard F, Bulla L, Brandt F, Kohout O, Steinlechner F, Fickler R, Malik M, Guryanova Y, Ursin R, and Huber M 2019 *Phys. Rev. X* **9** 041042
[12] Doda M, Huber M, Murta G, Pivoluska M, Plesch M, and Vlachou C 2021 *Phys. Rev. Appl.* **15** 034003
[13] Friis N, Vitagliano G, Malik M, and Huber M 2019 *Nat. Rev. Phys.* **1** 72
[14] Agnew M, Leach J, McLaren M, Roux F S, and Boyd R W 2011 *Phys. Rev. A* **84** 062101
[15] Gross D, Liu Y K, Flammia S T, Becker S, and Eisert J 2010 *Phys. Rev. Lett.* **105** 150401
[16] Giovannini D, Romero J, Leach J, Dudley A, Forbes A, and Padgett M J 2013 *Phys. Rev. Lett.* **110** 143601
[17] Bent N, Qassim H, Tahir A A, Sych D, Leuchs G, Sánchez-Soto L L, Karimi E, and Boyd R W 2015 *Phys. Rev. X* **5** 041006
[18] Riofrio C A, Gross D, Flammia S T, Monz T, Nigg D, Blatt R, and Eisert J 2017 *Nat. Commun.* **8** 15305
[19] Bavaresco J, Herrera Valencia N, Klöckl C, Pivoluska M, Erker P, Friis N, Malik M, and Huber M 2018 *Nat. Phys.* **14** 1032
[20] Kong L J, Liu R, Qi W R, Wang Z X, Huang S Y, Tu C, Li Y, and Wang H T 2020 *Chin. Phys. Lett.* **37** 034204
[21] Sahoo S N, Chakraborti S, Pati A K, and Sinha U 2020 *Phys. Rev. Lett.* **125** 123601
[22] Li Y, Huang S Y, Wang M, Tu C, Wang X L, Li Y, and Wang H T 2023 *Phys. Rev. Lett.* **130** 050805
[23] Liao S K, Cai W Q, Handsteiner J, Liu B, Yin J, Zhang L, Rauch D, Fink M, Ren J G, Liu W Y *et al.* 2018 *Phys. Rev. Lett.* **120** 030501
[24] Yin J, Cao Y, Li Y H, Liao S K, Zhang L, Ren J G, Cai W Q, Liu W Y, Li B, Dai H *et al.* 2017 *Science* **356** 1140
[25] Wootters W K and Zurek W H 1982 *Nature* **299** 802
[26] LeCun Y, Bengio Y, and Hinton G 2015 *Nature* **521** 436
[27] Goy A, Arthur K, Li S, and Barbastathis G 2018 *Phys. Rev. Lett.* **121** 243902
[28] Zhang Z, Wang F, Min Q, Jin Y, and Situ G 2024 *Opt. Lett.* **49** 6129
[29] Giordani T, Suprano A, Polino E, Acanfora F, Innocenti L, Ferraro A, Paternostro M, Spagnolo N, and Sciarrino F 2020 *Phys. Rev. Lett.* **124** 160401
[30] Xu P, Tong X, Zeng Z, Liu S, and Zhao D 2024 *Chin. Phys. Lett.* **41** 074201
[31] Wang Q, Liu J, Lyu D, and Wang J 2024 *Light Sci. Appl.* **13** 10
[32] Zhang Z W, Yang S, Wu Y H, Liu C X, Han Y M, Lee C H, Sun Z, Li G J, and Zhang X 2020 *Chin. Phys. Lett.* **37** 018401

[33] Torlai G, Mazzola G, Carrasquilla J, Troyer M, Melko R, and Carleo G 2018 *Nat. Phys.* **14** 447
[34] Carleo G, Nomura Y, and Imada M 2018 *Nat. Commun.* **9** 5322
[35] Ahmed S, Sánchez Muñoz C, Nori F, and Kockum A F 2021 *Phys. Rev. Lett.* **127** 140502
[36] Lu H, Myilswamy K V, Bennink R S, Seshadri S, Alshaykh M S, Liu J, Kippenberg T J, Leaird D E, Weiner A M, and Lukens J M 2022 *Nat. Commun.* **13** 4338
[37] Tiunov E S, Tiunova V V, Ulanov A E, Lvovsky A I, and Fedorov A K 2020 *Optica* **7** 448
[38] Zhao J, Wang M, Huang S Y, Ge Y, Tu C, Li Y, and Wang H T 2025 *Laser Photonics Rev.* **19** 2400720
[39] Wang F, Bian Y, Wang H, Lyu M, Pedrini G, Osten W, Barbastathis G, and Situ G 2020 *Light Sci. Appl.* **9** 77
[40] Mair A, Vaziri A, Weihs G, and Zeilinger A 2001 *Nature* **412** 313
[41] McLaren M, Agnew M, Leach J, Roux F S, Padgett M J, Boyd R W, and Forbes A 2012 *Opt. Express* **20** 23589
[42] Krenn M, Fickler R, Huber M, Lapkiewicz R, Plick W, Ramelow S, and Zeilinger A 2013 *Phys. Rev. A* **87** 012326
[43] Walborn S P, Pádua S, and Monken C H 2005 *Phys. Rev. A* **71** 053812
[44] Oripov B G, Rampini D S, Allmaras J, Shaw M D, Nam S W, Korzh B, and McCaughan A N 2023 *Nature* **622** 730